

This copy is for your personal, non-commercial use only.

If you wish to distribute this article to others, you can order high-quality copies for your colleagues, clients, or customers by [clicking here](#).

Permission to republish or repurpose articles or portions of articles can be obtained by following the guidelines [here](#).

The following resources related to this article are available online at www.sciencemag.org (this information is current as of August 24, 2010):

Updated information and services, including high-resolution figures, can be found in the online version of this article at:

<http://www.sciencemag.org/cgi/content/full/329/5994/967>

Supporting Online Material can be found at:

<http://www.sciencemag.org/cgi/content/full/329/5994/967/DC1>

This article **cites 27 articles**, 9 of which can be accessed for free:

<http://www.sciencemag.org/cgi/content/full/329/5994/967#otherarticles>

This article appears in the following **subject collections**:

Development

<http://www.sciencemag.org/cgi/collection/development>

20. T. Pizzari, C. K. Cornwallis, H. Løvlie, S. Jakobsson, T. R. Birkhead, *Nature* **426**, 70 (2003).
21. M. Olsson, R. Shine, T. Madsen, A. Gullberg, H. Tegelstrom, *Nature* **383**, 585 (1996).
22. A. Pusey, M. Wolf, *Trends Ecol. Evol.* **11**, 201 (1996).
23. T. Tregenza, N. Wedell, *Nature* **415**, 71 (2002).
24. J. Merilä, L. E. B. Kruuk, B. C. Sheldon, *Nature* **412**, 76 (2001).
25. T. Veen *et al.*, *Nature* **411**, 45 (2001).
26. J. Merilä, B. C. Sheldon, S. C. Griffith, *Ann. Zool. Fenn.* **40**, 269 (2003).
27. W. G. Eberhard, *Female Control: Sexual Selection by Cryptic Female Choice* (Princeton Univ. Press, Princeton, NJ, 1996).
28. S. C. Griffith, *Am. Nat.* **169**, 274, discussion 282 (2007).
29. We thank T. Birkhead, R. Brooks, R. Calsbeek, S. Immler, S. Ulstrand, D. Westneat, and M. Whiting for comments on the manuscript. This work was supported by Discovery Grants DP0770889 (S.R.P.) and DP0881019 (S.C.G.) from the Australian Research Council, a L'Oréal for Women in Science Fellowship (S.R.P.), and the Save the Gouldian

Fund. The Animal Care and Ethics Committee of Macquarie University approved this research.

Supporting Online Material

www.sciencemag.org/cgi/content/full/329/5994/964/DC1
Materials and Methods

Fig. S1
Table S1
References

17 May 2010; accepted 7 July 2010
10.1126/science.1192407

Cell Lineage Reconstruction of Early Zebrafish Embryos Using Label-Free Nonlinear Microscopy

Nicolas Olivier,^{1*} Miguel A. Luengo-Oroz,^{2*} Louise Duloquin,^{3*} Emmanuel Faure,⁴ Thierry Savy,⁴ Israël Veilleux,¹ Xavier Solinas,¹ Delphine Débarre,¹ Paul Bourguine,^{4,5} Andrés Santos,² Nadine Peyrieras,^{3,6†} Emmanuel Beaurepaire^{1†}

Quantifying cell behaviors in animal early embryogenesis remains a challenging issue requiring in toto imaging and automated image analysis. We designed a framework for imaging and reconstructing unstained whole zebrafish embryos for their first 10 cell division cycles and report measurements along the cell lineage with micrometer spatial resolution and minute temporal accuracy. Point-scanning multiphoton excitation optimized to preferentially probe the innermost regions of the embryo provided intrinsic signals highlighting all mitotic spindles and cell boundaries. Automated image analysis revealed the phenomenology of cell proliferation. Blastomeres continuously drift out of synchrony. After the 32-cell stage, the cell cycle lengthens according to cell radial position, leading to apparent division waves. Progressive amplification of this process is the rule, contrasting with classical descriptions of abrupt changes in the system dynamics.

Although classical developmental biology is characterized by qualitative descriptions, recent work underlines the requirements for precise measurements to enable formal reconstruction integrating the genetic, molecular, and cellular levels of organization (1–3). The optimization of microscopy imaging techniques and improved data algorithmic processing are key issues in such reconstructions. Parallelized linear microscopy such as light-sheet fluorescence microscopy provides fast imaging but suffers from loss of information with depth (4). Point-scanning two-photon microscopy provides deeper imaging (5) but exhibits slower frame rate, compromising

automated individual cell tracking in whole organisms (6). Furthermore, the usual implementation of these two paradigms does not allow homogeneous illumination in spherical samples, leading to a difficult tradeoff between the detection of deep structures and illumination-induced perturbation in outer layers. Finally, relying on fluorescent staining of biological structures brings additional artifacts and limitations. Exploiting the intrinsic optical nonlinear properties of the sample is a valuable, although challenging, alternative. Second-harmonic generation (SHG) is obtained from dense noncentrosymmetric structures such as oriented microtubule assemblies (7–9), including mitotic spindles (8, 10). Third-harmonic generation (THG) is obtained from optical heterogeneities (11)—such as the interface between an aqueous medium and a lipidic, mineralized, or absorbing structure (12)—and allows morphological imaging of small organisms (10, 13).

Here, we show that combining SHG and THG imaging of unlabeled embryos with a scanning scheme matching embryo morphology provides adequate three-dimensional (3D) imaging over time for the automated reconstruction of cell behavior during zebrafish embryo cleavage stages (14). Ad hoc image analysis strategies for cell position, division, and shape identification were used to produce a complete and validated lineage

tree for a cohort of six zebrafish embryos until the 1000-cell stage, annotated with minute-level division timing, micrometer-accuracy cell coordinates, and shape characteristics. These data provided a quantitative spatiotemporal description of the wave-like division cycles and allowed the construction of a prototypic digital blastula. The cycle duration of sister cells exhibited variability that did not correlate with cell volume, revealing unexpected cell division asynchrony and asymmetry from the first division cycles and leading to increasing cell heterogeneity by the time of midblastula transition (MBT) (14).

An appropriate image acquisition scheme was devised to provide high-resolution time-lapse imaging of intrinsic SHG and THG signals (Fig. 1 and supporting online material). Excitation in the 1.2- μm range reduced nonlinear endogenous absorption by the sample and allowed simultaneous two-photon-excited fluorescence (2PEF) imaging of red fluorescent proteins (Fig. 1, B and C) for control experiments. When imaging a spherical embryo, scattering and aberrations typically result in reduced signal at the center of each plane (Fig. 1E). We therefore scanned each plane of a half-sphere along a spiral trajectory with variable speed to spend more time imaging the innermost cells (Fig. 1, D to F, and fig. S1). This conformal strategy provided optimal acquisition time and minimal photoperturbation (fig. S2). SHG and THG signals were co-optimized by using rotating linear incident polarization. In addition, because THG contrast from a specific structure depends on its size relative to the focal volume (15), moderate focusing (3.5- μm Z-resolution) was used to highlight cell interface compared with smaller subcellular structures (Fig. 2D).

Combining the conformal scanning scheme described above, sensitive detection, infrared excitation wavelength, and appropriate focusing and polarization conditions allowed homogenous detection of mitotic spindles and cell and tissue phenotypic features in the whole unlabeled zebrafish embryo during cleavage stages. The blastoderm was contained in a half sphere of 440- μm radius imaged with a temporal resolution of 80 s and a volumetric pixel size of 2 by 2 by 4 μm , suitable for further automated reconstruction of the cell lineage tree.

The intrinsic THG signal revealed a number of structures and dynamic processes (Fig. 2, A to J, and movies S1 to S6) and highlighted cell contours even better than membrane staining by

¹Laboratory for Optics and Biosciences, Ecole Polytechnique, CNRS, INSERM, Palaiseau, France. ²Biomedical Image Technologies, Universidad Politécnica de Madrid, and Biomedical Research Center in Bioengineering, Biomaterials, and Nanomedicine (CIBER-BBN), Madrid, Spain. ³Neurobiologie et Développement, Institut de Neurobiologie Alfred Fessard, CNRS, Gif/Yvette, France. ⁴Centre de Recherche en Epistémologie Appliquée, Ecole Polytechnique, CNRS, Paris, France. ⁵Réseau National des Systèmes Complexes, 57-59 rue Lhomond, Paris, France. ⁶Institut des Systèmes Complexes Paris Ile-de-France, 57-59 rue Lhomond, Paris, France.

*These authors contributed equally to this work.

†To whom correspondence should be addressed. E-mail: nadine.peyrieras@inaf.cnrs-gif.fr (N.P.); emmanuel.beaurepaire@polytechnique.edu (E.B.)

farnesylated mCherry, indicating the presence of a sizeable intercellular space as corroborated by numerical simulations (Fig. 2, K to M). Higher-numerical aperture THG imaging produced signal discontinuities or double interfaces at cell boundaries (Fig. 2D), indicating local distance variation between cells. This interpretation is reinforced by the absence of THG signal from the lateral junction of the enveloping layer (EVL) (fig. S3). THG also allowed visualizing trafficking phenomena, including cell membrane completion at the 32-cell

stage (movie S2) and nuclear envelope dynamics during mitosis (movie S3). In addition, when embryos were overilluminated, photo damage correlated with enhanced intracellular THG signal, serving as a control of embryo physiological condition (fig. S2). THG also revealed yolk lipid platelets interface and allowed visualizing the phenomenology of cytoplasmic streams during the first cell cycles (movie S1). Combining THG/SHG/2PEF in *βactin:H2B/mcherry* transgenic embryos (16) allowed correlating SHG and THG signals with

mitosis phases (Fig. 2, G to I, and movie S4). As shown in Fig. 2O, SHG intensity exhibited a nearly Gaussian temporal profile peaking at metaphase, providing measurement for division timing and cell cycle duration with subminute accuracy.

We designed an original image processing methodology for automatically extracting cell position, membrane geometry, and cell lineage, taking advantage of mitosis metasynchrony and limited cell displacements during the first 10 division cycles (fig. S4 and movies S5 and S6).

Fig. 1. Conformal scanning harmonic microscopy scheme. (A) Schematized zebrafish embryo imaged from the animal pole. (B) Sample mounting for upright microscopy; excitation (Exc.) and detection geometry (2PEF epidetected, THG-SHG transmitted). (C) Energy diagrams and wavelengths involved. (D) Lateral position (left) and depth (right) of the focal point inside a spherical sample when using raster scanning (top) versus conformal scanning (bottom). (E) THG imaging with raster (top) and spiral scanning (bottom). Acquisition time is 5 s. Scale bar, 100 μm . (F) XZ two-photon excitation using raster (top) and conformal (bottom) scan patterns with preferential energy delivery to the deepest regions in the conformal scheme.

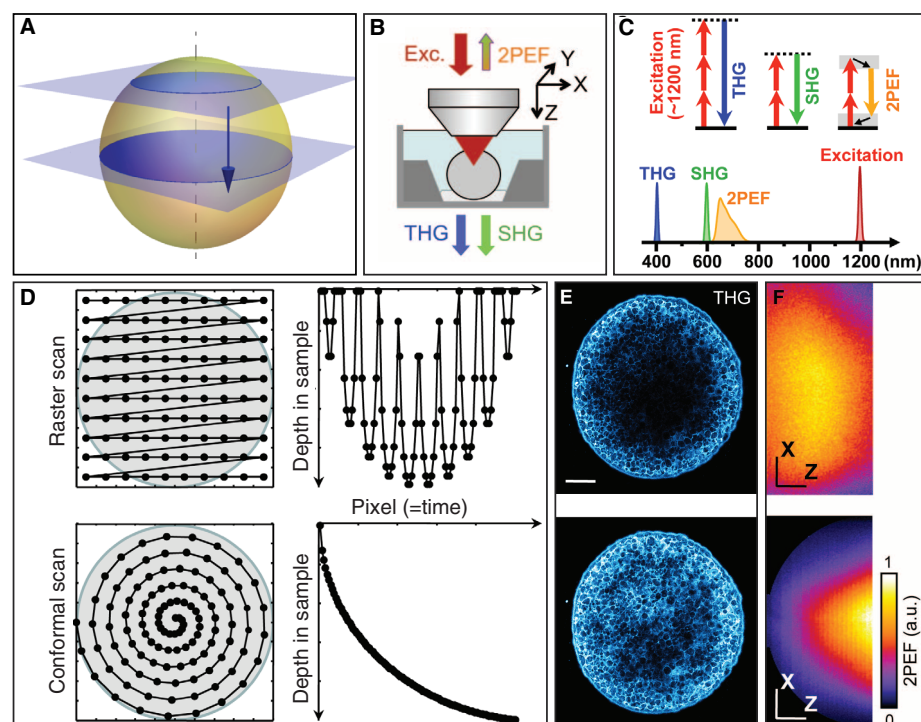
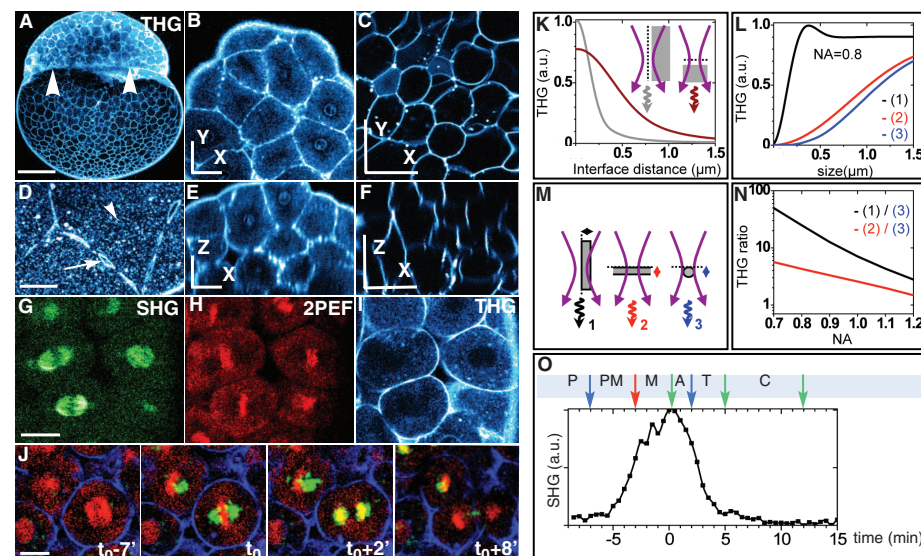


Fig. 2. THG and SHG signals in the zebrafish embryo during cleavage stages. (A) Sagittal THG image, 512-cell stage, animal pole to the top; white arrowheads indicate yolk-blastoderm interface. Scale bar, 200 μm . (B and C) THG XY image and (E and F) ZX projection. (B and E) Blastoderm cells imaged with 0.8 numerical aperture (NA) excitation, 64-cell stage. Scale bars, 50 μm . (C and F) Yolk platelets imaged under conditions similar to B and E. (D) THG XY image of blastoderm cells with 1.2 NA excitation; white arrow points to double interface, arrowheads point to intracellular organelles. Scale bar, 30 μm . (G to I) *βactin:H2B/mcherry* transgenic imaged with SHG-2PEF-THG. Scale bar, 20 μm . (J) Merged SHG-2PEF-THG, temporal sequence. (K) Calculations of THG from lateral (gray) and axial (brown) interfaces as a function of position, modeling the nuclear membrane signal. (L to N) Calculations of THG from heterogeneities, modeling cell boundaries (black, red) and vesicles (blue). (N) THG ratio between a 0.6- μm slab and a 0.4- μm diameter sphere as a function of NA. Using moderate NA, enhanced cell interfaces signal compared to small organelles. (O) Evolution of SHG signal intensity during mitosis. Prophase, P; prometaphase, PM; metaphase, M; telophase, T; and cytokinesis, C, revealed by THG-SHG-2PEF signals (movie S4).



This allowed measurements along the cell lineage tree throughout cleavage (17) until the onset of MBT (18). Mitoses were detected from the

SHG channel by compressing the data into 10 volumes corresponding to cell cycles and detecting in each volume the expected number of SHG

spots corresponding to cell divisions (2, 4, 8...) (Fig. 3A and movie S7). A distance rule respecting the symmetric and limited displacement of

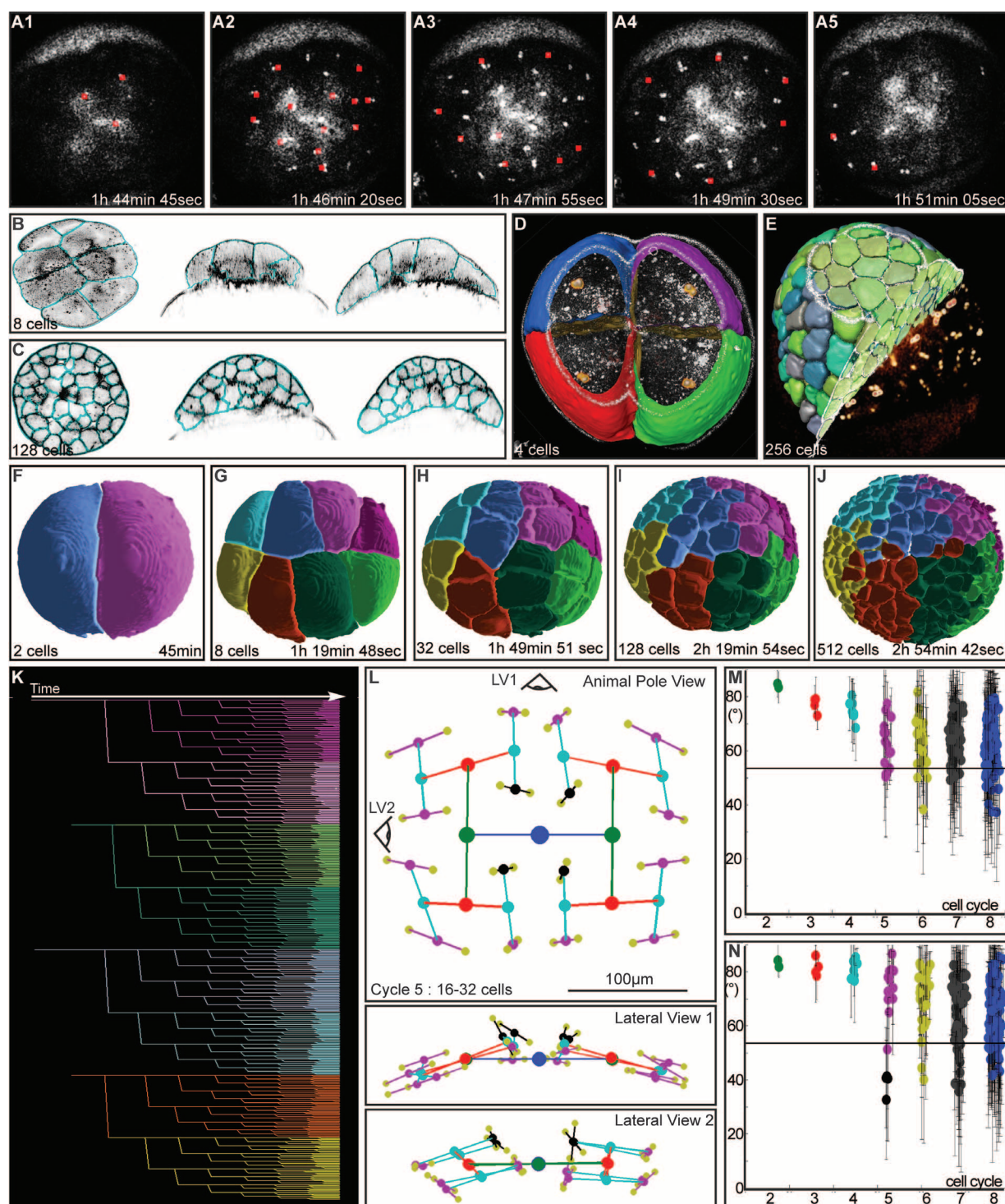


Fig. 3. Automated reconstruction of the cell lineage tree for a cohort of zebrafish early blastulas. (A) SHG spot detection (red) overlaid to XY projections of SHG images; A1 to A5 encompass cell cycle 5 (with cell division 1 at 45 min); see movie S8. (B and C) THG image segmentation at the 8-cell stage (B) and 128-cell stage (C); see movie S9. (D and E) Reconstruction of 4-cell stage (D) and 256-cell stage (E) embryos. In white, raw THG signal; orange, detected SHG spots; colors, segmented cell contours. (F to J) Digital embryo from 1-cell stage to 512-cell stage. See movie S10. (K) Flat representation of

the lineage tree with eight-cell stage clones; same colors as in (G) to (J). (L) Spatial deployment of the cell lineage up to cycle 5. (Top) Animal pole view. (Bottom) Lateral views. See movie S11 and fig. S6. (M) Angle between successive sister cells dipoles, in degrees. 55° (black line) corresponds to random orientation. (N) Angle between sister cells dipoles and the normal to the embryo surface. Cells divided tangentially to the embryo surface until cycle 5 (16 to 32 cells). At cycle 5, the four central blastomeres [shown in black in (L) and (N)] divided orthogonally to the surface.

daughter cells after mitosis was then used to link consecutive sequences. Finally, accurate cell cycle timing was obtained by fitting time-dependent SHG intensity to a Gaussian function (Fig. 2O). The lineage tree validation is a critical step as tracking errors propagate along the tree. Validation was performed using an interactive visualization interface that allowed comparing raw and reconstructed data at each cell cycle before processing the next one (movie S8). This strategy

provided error-free lineage trees with minimal human intervention (fig. S5). Cell shapes were then extracted from THG images by using cells' spatial coordinates as seeds to perform a region growing-based contour detection. A rough shape approximation was first obtained by building a Voronoi diagram, and membrane detection was refined using a viscous watershed algorithm (19) (movie S9 and Fig. 3, B to E). Data sets from six different embryos were processed to obtain the

corresponding digital blastulas (Fig. 3, fig. S5, and movies S10 to S13).

The phenomenological reconstruction allowed a systematic analysis of spatiotemporal correlations between cell position, cell cycle duration, mitosis duration, cell volume, and cell division orientation. Cells during cycles 1 to 4 were constrained by the absence of basal plasma membrane contacting the yolk, and divisions displayed the known stereotyped orientation with

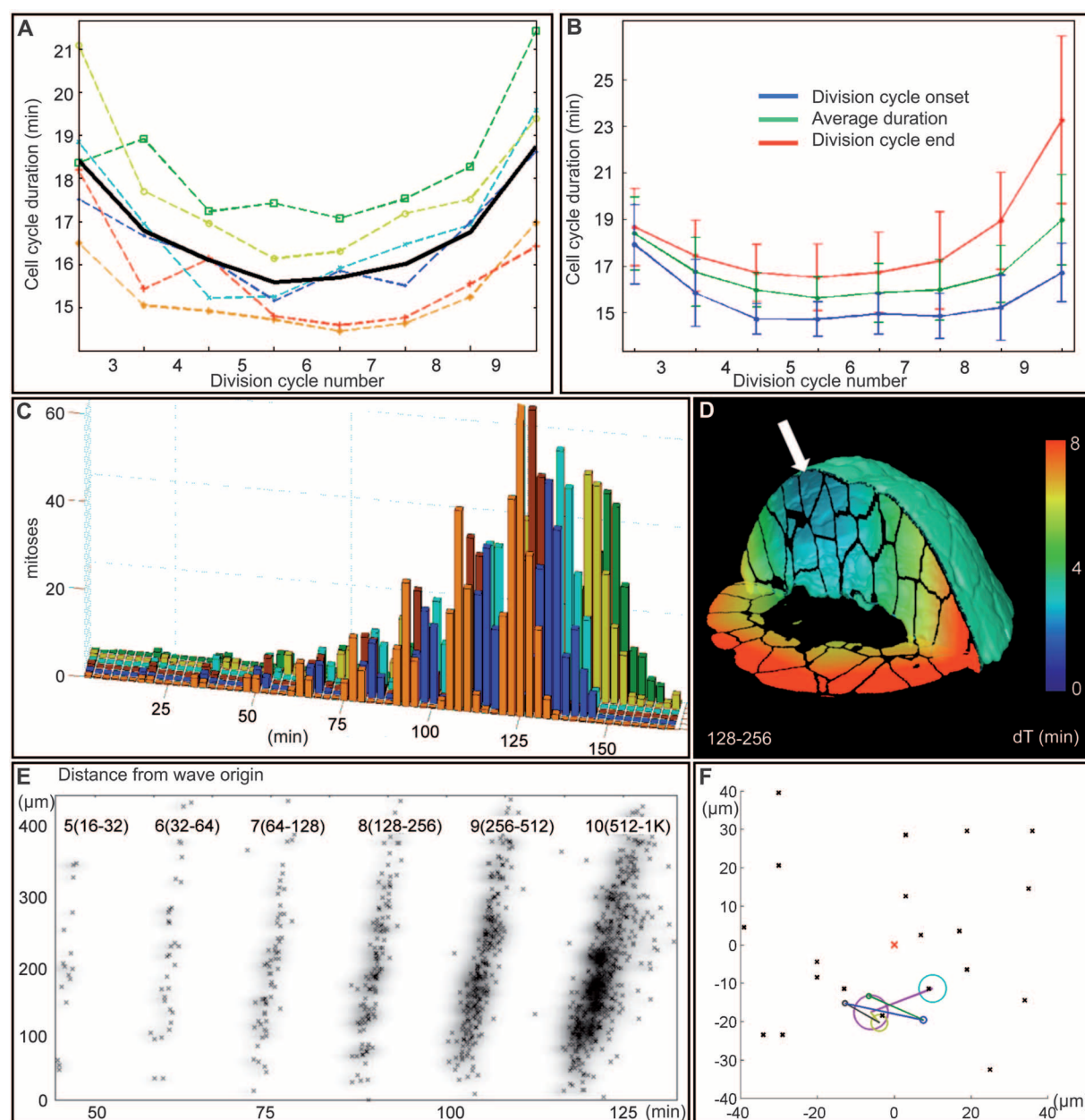


Fig. 4. Data statistical homogeneity, local features, and global patterns. (A) Mean cell cycle duration (metaphase-to-metaphase) from cycles 2 to 10 for six embryos (black line, average). (B) Mean cell cycle duration (green) compared with cycle duration at the beginning (blue) and at the end (red) of the division cycle, averaged for six embryos. (C) Temporal histogram of mitoses in six embryos. (D) Spatiotemporal representation of the mitotic pseudo-wave at

cycle 8; time ranges from 0 min (blue, cycle onset) to 8 min (red, cycle end); white arrow points to the pseudo-wave origin. (E) Scatter plot of mitosis time (SHG peak at metaphase) as a function of distance to the pseudo-wave origin. (F) XY projection of the position of the pseudo-wave origin for cycles 5 to 10 with respect to the animal pole (red cross) and other mitoses at cycle 10 (black crosses). Data for five other embryos are in the supporting online material.

little fluctuation from one embryo to the other (Fig. 3M). Division orientation at cycle 5 started exploring one more spatial direction at 90° relative to the previous division, thus allowing the formation of a partially double-layered blastoderm (Fig. 3, L and N). This quantitative observation contrasts with the classical description presenting the 32-cell stage as a single cell layer (14). From divisions 5 to 8, larger fluctuations occurred in division orientation, resulting in progressively more random orientations (Fig. 3N and fig. S6). By averaging and registering six different embryos, we constructed a prototype of the lineage spatiotemporal deployment (fig. S6 and movie S10). From cycle 3 to cycle 9, cell displacements were limited to cytokinesis, and displacement speed from one division to the other remained constant (fig. S7), suggesting that biochemical dynamics (20, 21) do not impact cell displacements until MBT, quantitatively supporting previous observations (18). Consistently, the clones corresponding to the first eight blastomeres observed at the 512-cell stage remained clustered (Fig. 3, F to J, and movie S10).

In the temporal domain, the main dynamical change was the evolution of cell cycle duration as previously observed (22). The cell cycle shortened until division 5 (18.5 ± 1.5 min to 15.5 ± 1 min), followed by lengthening until division 10 (up to 18.5 ± 1.5 min) (Fig. 4A). The minimum value correlated with plasma membrane completion at the 32-cell stage, suggesting a specific regime for the division of the large early blastomeres (23, 24). Continuous cell cycle lengthening thereafter is hypothesized to result from the degradation of maternal products and S-phase lengthening (21). Furthermore, as early as the 4-cell stage, cell divisions did not occur synchronously, and the delay measured between the first and last division at each cell cycle increased continuously through cleavages (Fig. 4, B and C).

In addition, after the 32-cell stage, cell cycle lengthening increased with the physical distance from the blastoderm surface (Fig. 4, D and E, and figs. S8 to S11), so that in the particular case of sister cells, the deeper tended to divide later than her sister located closer to the surface (fig. S13). We hypothesize that this feature correlates with deposition of maternal components by cytoplasmic streams (movie S1) that might have produced a concentration gradient. In any case, fluctuation in sister cells' division timing and steady lengthening in cell cycle duration as a function of cell position relative to the blastoderm surface are sufficient to explain the progressive appearance of a global wave-like pattern of radial division (Fig. 4, D and E). Calculating the position of this pseudo-wave origin relative to the animal pole indicated an early symmetry breaking variably amplified in some cases (fig. S14). A discussion of the cell division patterns during cleavage stages must also take into account the formation of the yolk syncytial layer (YSL) (25). We observed that YSL nuclei typically individualized at the 512-cell stage and underwent three

division cycles with an average timing of 20 to 30 min and displaying a peripheral pattern, thus differing from the radial pattern observed in the blastoderm (movies S14 to S16 and figs. S15 and 16). YSL formation is known to display phenotypic variability (26), but extreme cases of artifactual YSL formation were observed in embryos mechanically constrained by the mounting medium (movie S16 and fig. S17). Altogether, our observations suggest that there is no switch from a radial toward a peripheral pseudo-wave pattern in the blastoderm, in contrast to a recent proposal by Keller *et al.* (4).

Cell volume measurements indicated that up to cycle 10, the nucleocytoplasmic ratio (N/C) was unlikely to trigger cell cycle lengthening as we observed cell volume variability, including random fluctuation between sister cells, with no correlation to cycle duration (figs. S11 and S12). According to other studies, N/C becomes an important factor at later developmental stages (18). Indeed, a pause in cell cycle, regulated by N/C, is described as one of the most prominent features of the MBT (27). This means that by MBT, the N/C variability generated earlier could act as a local fluctuation factor, breaking the global pseudo-wave pattern. Cell cycle lengthening, both globally and as a function of cell position, is the main parameter that should be taken into account for further modeling zebrafish embryo cleavage morphogenesis. Continuity and amplification of the process are the rule, rather than the classically described abrupt changes from synchrony to metasyncrony and asynchrony (14).

Harmonic time-lapse microscopy provides in toto imaging, enabling automated and validated reconstruction of the zebrafish embryo lineage tree during the cleavage period. Because the reconstruction scheme is based on cell cycle metasyncrony and limited cell displacements, we provide a quantitative assessment that cell intrinsic motility does not arise before cell cycle 10, described as the MBT stage (18). The framework presented here automates the phenomenological reconstruction of animal early embryogenesis without the use of fluorescent staining. Conformal acquisition with excitation power and scanning speed matching specimen morphology makes point-scanning multiphoton microscopy an excellent strategy for deep embryo imaging. We anticipate that combining harmonic and fluorescent signals in conformal scanning time-lapse microscopy will provide optimal data sets to achieve the automated tracking of cell trajectories and cell divisions throughout vertebrate embryogenesis. Single-cell analysis along the lineage tree is necessary to provide relevant spatial and temporal correlations underlying emerging patterns. Most of developmental biology still relies on visual inspection and manual work to achieve limited cell tracking, and recent studies have provided only a global estimation of cell movements. In this context, we expect our framework to establish standards in terms of measurements precision and accuracy of automated algorithmic

segmentation and tracking procedures. The quantitative phenomenological reconstruction of the zebrafish embryo cleavage period provided here should serve as a reference for further analysis of the interplay between nano- (molecular and genetic) and macro- (biomechanics) level dynamics.

References and Notes

1. C. Zimmer *et al.*, *IEEE Signal Process. Mag.* **23**, 54 (2006).
2. D. Muzzey, A. van Oudenaarden, *Annu. Rev. Cell Dev. Biol.* **25**, 301 (2009).
3. A. C. Oates, N. Gorfinkel, M. González-Gaitán, C. P. Heisenberg, *Nat. Rev. Genet.* **10**, 517 (2009).
4. P. J. Keller, A. D. Schmidt, J. Wittbrodt, E. H. Stelzer, *Science* **322**, 1065 (2008).
5. F. Helmchen, W. Denk, *Nat. Methods* **2**, 932 (2005).
6. A. McMahon, W. Supatto, S. E. Fraser, A. Stathopoulos, *Science* **322**, 1546 (2008).
7. W. R. Zipfel *et al.*, *Proc. Natl. Acad. Sci. U.S.A.* **100**, 7075 (2003).
8. P. J. Campagnola *et al.*, *Biophys. J.* **82**, 493 (2002).
9. A. C. Kwan, D. A. Dombeck, W. W. Webb, *Proc. Natl. Acad. Sci. U.S.A.* **105**, 11370 (2008).
10. C.-K. Sun *et al.*, *J. Struct. Biol.* **147**, 19 (2004).
11. Y. Barad, H. Eisenberg, M. Horowitz, Y. Silberberg, *Appl. Phys. Lett.* **70**, 922 (1997).
12. D. Oron *et al.*, *J. Struct. Biol.* **147**, 3 (2004).
13. D. Débarre *et al.*, *Opt. Lett.* **29**, 2881 (2004).
14. C. B. Kimmel, W. W. Ballard, S. R. Kimmel, B. Ullmann, T. F. Schilling, *Dev. Dyn.* **203**, 253 (1995).
15. D. Débarre, W. Supatto, E. Beaurepaire, *Opt. Lett.* **30**, 2134 (2005).
16. J. P. Levraud *et al.*, *J. Immunol.* **178**, 4385 (2007).
17. W. Tadros, H. D. Lipshitz, *Development* **136**, 3033 (2009).
18. D. A. Kane, C. B. Kimmel, *Development* **119**, 447 (1993).
19. C. Vachier, F. Meyer, *J. Math. Imaging Vis.* **22**, 251 (2005).
20. S. Mathavan *et al.*, *PLoS Genet.* **1**, 260 (2005).
21. A. F. Schier, *Science* **316**, 406 (2007).
22. D. A. Kane, R. M. Warga, C. B. Kimmel, *Nature* **360**, 735 (1992).
23. T. Yabe *et al.*, *PLoS Genet.* **5**, e1000518 (2009).
24. E. W. Abrams, M. C. Mullins, *Curr. Opin. Genet. Dev.* **19**, 396 (2009).
25. C. B. Kimmel, R. M. Warga, T. F. Schilling, *Development* **108**, 581 (1990).
26. J. P. Trinkaus, *J. Exp. Zool.* **265**, 258 (1993).
27. X. M. Lu, J. M. Li, O. Elemento, S. Tavazoie, E. F. Wieschaus, *Development* **136**, 2101 (2009).
28. We thank G. Lutfalla for pAct26H2B/mCherry, pAct26mCherry-F DNA constructs, and transgenic fish lines. We thank P. Herbolme, C. Little, J.-L. Martin, H. Myllykallio, and J.-L. Rubio for critical reading of the manuscript. This work was supported by Direction Générale de l'Armement, Agence Nationale de la Recherche, FP6 New Emerging Science and Technology program, Association pour le Recherche Contre le Cancer, Egide Picasso France-Spain, and Fondation Louis D., Institut de France. Patent application PCT/FR2010/050173 describes the combination of conformal acquisition and beam conditioning in scanning microscopy of 3D objects.

Supporting Online Material

www.sciencemag.org/cgi/content/full/329/5994/967/DC1
Materials and Methods

Figs. S1 to S17

References

Movies S1 to S16

11 March 2010; accepted 7 July 2010
10.1126/science.1189428